

Modeling of Cyclic Shear-Flexure Interaction in Reinforced Concrete Structural Walls. II: Experimental Validation

Kristijan Kolozvari, Ph.D.¹; Thien A. Tran, Ph.D.²; Kutay Orakcal, Ph.D.³; and John W. Wallace, Ph.D., P.E., M.ASCE⁴

Abstract: This paper presents the experimental calibration and validation of the analytical wall model that incorporates interaction between shear and flexural responses under cyclic loading conditions described in the companion paper. The model is calibrated and validated against detailed experimental data obtained from tests on five moderately slender reinforced concrete wall specimens that experienced significant levels of shear-flexure interaction. Test measurements were processed to allow for detailed comparisons between the predicted and measured wall responses at various locations and response levels. Response comparisons reveal that the proposed analytical model captures the experimentally measured nonlinear shear deformations and their coupling with flexural deformations throughout the cyclic loading history. In addition, the analytical results successfully represent various experimentally measured responses, such as lateral-load versus wall-top-displacement relations, magnitudes and distributions of deformations associated with shear and flexure, and local responses including flexural rotations, vertical strains, and concrete crack orientations. Based on the comparisons presented, model capabilities are assessed and future model improvements are suggested. DOI: [10.1061/\(ASCE\)ST.1943-541X.0001083](https://doi.org/10.1061/(ASCE)ST.1943-541X.0001083). © 2014 American Society of Civil Engineers.

Author keywords: Reinforced concrete walls; Analytical modeling; Shear-flexure interaction; Model validation; Analysis and computation.

Introduction

A large percentage of reinforced concrete (RC) walls in buildings with less than ten stories can be classified as moderately slender, with wall height-to-length ratios (aspect ratios) or shear-span-to-depth ratios ($M_u/V_u l_w$) ranging between approximately 1.5 and 3.0. For these moderate-aspect-ratio walls, flexural yielding is expected; however, nonlinear shear deformations can be significant and lead to reduced stiffness and reduced load and deformation capacity. According to experimental evidence, the interaction between flexural and shear deformations exists even for relatively slender RC walls with aspect ratios of 3.0 and 4.0, with shear deformations contributing to lateral deformations by approximately 30% and 10% of the first story and roof-level lateral displacement, respectively (Barda et al. 1976; Massone and Wallace 2004). Experimental results have shown that nonlinear shear deformations for RC walls with aspect ratios of 1.5 and 2.0 contribute as much as 50% and 30% of the wall top displacement, respectively (Tran and Wallace 2012).

The majority of available analytical models for RC walls usually do not incorporate this experimentally observed shear-flexure

interaction (SFI) and describe wall shear behavior using ad hoc force deformation rules defined independently from the flexural modeling parameters (e.g., Vulcano and Bertero 1987; Orakcal et al. 2004). Various approaches have been proposed to capture the experimentally observed coupling between nonlinear flexural and shear modes of behavior, such as the empirical (or semiempirical) modeling approach proposed by Beyer et al. (2011), the strut-and-tie (truss) model developed by Panagiotou et al. (2011), and models that incorporate SFI directly at the model element level (e.g., Petrangeli et al. 1999; Massone et al. 2006, 2009; Jiang and Kurama 2010; Fischinger et al. 2012). However, modeling approaches available in the literature that incorporate SFI behavior have not been sufficiently validated against both global (load-displacement) responses and local deformation characteristics (rotations, curvatures, strains) because of a lack of detailed experimental data for walls with significant interaction. There is a need for a relatively simple yet mechanical (physical) model capable of capturing the interaction between axial, flexural, and shear responses in RC structural walls under reversed cyclic loading conditions, one that is experimentally validated for a range of both global and local response amplitudes using data from heavily instrumented tests of moderate-aspect-ratio wall specimens.

Based on the aforementioned shortcoming, analytical and experimental studies were conducted to develop, calibrate, and validate an analytical model that captures cyclic interaction between nonlinear shear and flexural responses of RC walls. A brief description of the modeling approach developed and the constitutive relationships implemented is provided, followed by detailed calibration and validation studies using experimental data obtained from five moderately slender (of aspect ratio 1.5 and 2.0) and heavily instrumented RC wall specimens that experienced significant levels of SFI; a detailed description of the model and the sensitivity of analytical results to modeling parameters are presented in the companion paper (Kolozvari et al. 2014). Comprehensive comparisons between experimental and model results at both global and

¹Senior Engineer and Analyst, Saiful/Bouquet Structural Engineers Inc., 155 N Lake Ave., Suite 600, Pasadena, CA 91101 (corresponding author). E-mail: kolozvari@yahoo.com

²Postdoctoral Researcher, Dept. of Civil and Environmental Engineering, Univ. of California, Los Angeles, CA 90095-1593. E-mail: thientran@ucla.edu

³Associate Professor, Dept. of Civil Engineering, Bogazici Univ., Bebek-Istanbul 34342, Turkey. E-mail: kutay.orakcal@boun.edu.tr

⁴Professor, Dept. of Civil and Environmental Engineering, Univ. of California, Los Angeles, CA 90095-1593. E-mail: wallacej@ucla.edu

Note. This manuscript was submitted on August 31, 2013; approved on March 20, 2014; published online on July 18, 2014. Discussion period open until December 18, 2014; separate discussions must be submitted for individual papers. This paper is part of the *Journal of Structural Engineering*, © ASCE, ISSN 0733-9445/04014136(12)/\$25.00.

local response levels indicate that the model reasonably captures a broad range of experimental results (but not failure modes associated with rebar buckling and lateral instability) and provides a flexible framework for future improvements.

Analytical Model

The analytical model proposed, called SFI-MVLEM (shear-flexure interaction multiple vertical line element model; [Koložvari et al. 2014](#)), incorporates RC panel behavior into a two-dimensional macroscopic fiber model formulation (multiple vertical line element model, MVLEM, [Orakcal et al. 2004](#)) in which shear behavior is uncoupled from flexural behavior and is necessarily described using ad hoc force-deformation rules. In the present model, each uniaxial (macrofiber) element used to describe the axial/flexural behavior in the original formulation of MVLEM is replaced with a RC panel element subjected to membrane actions (Fig. 1). Therefore, coupling of axial and shear responses is achieved at the panel (macrofiber) level, which further allows coupling of axial/flexural and shear responses at the model element level. For each RC panel element, axial strain in the vertical (longitudinal) direction ϵ_y and shear strain γ_{xy} are calculated from displacements along six nodal degrees of freedom located at the top and the bottom level of a model element (Fig. 1), based on assumptions that plane sections remain plane and that shear strains are uniformly distributed along the length of the wall. In addition, using the horizontal (transverse) degrees of freedom assigned to each RC panel element (Fig. 1), axial strains in the horizontal direction ϵ_x are obtained assuming that the resultant horizontal axial stress σ_x (resulting from the contributions from concrete and reinforcing steel) is equal to zero; this assumption has been shown to be reasonable for walls with aspect ratio greater than 1.0 ([Massone et al. 2009](#)). The RC panel behavior is represented by a cyclic two-dimensional constitutive relationship described using a constitutive panel model formulation based on the fixed strut angle model (FSAM) developed by [Ulugtekin \(2010\)](#) but also including a shear resisting mechanism along concrete cracks. Similarly to the shear friction approach in ACI 318-11 Section 11.6.4 ([American Concrete Institute 2011](#)), shear resistance across a concrete crack consists of aggregate interlock effects and a dowel action of reinforcement. While in ACI 318-11 these effects are combined, in the implemented RC panel model, shear aggregate interlock and dowel action of reinforcement are described with two independent models to provide more flexibility in calibration of model results with experimentally observed behavior. Shear aggregate interlock effects are described using a friction-based, elasto-plastic model ([Orakcal et al. 2012](#)) characterized with the friction coefficient η , whereas the contribution of dowel action of vertical reinforcement is described using a linear-elastic constitutive model with shear

stiffness defined as a fraction of Young's modulus for steel via parameter α (stiffness parameter of the dowel action); therefore, parameters η and α of implemented shear resisting mechanisms require calibration against experimental results.

Biaxial stress-strain relationships are used to represent the behavior of concrete along fixed compression struts within each RC panel element, whereas the behavior of reinforcing steel is described by uniaxial stress-strain relationships applied along the directions of reinforcing steel bars. The constitutive relationship proposed by [Chang and Mander \(1994\)](#) was implemented to simulate the behavior of concrete along "fixed struts" [Fig. 2(a)]. In the panel model implemented, the original formulation of the Chang and Mander model was modified to represent behavioral features of concrete under biaxial loading via inclusion of parameters representing compression softening, defined by [Vecchio and Collins \(1993\)](#); hysteretic biaxial damage, defined by [Mansour et al. \(2002\)](#); and tension stiffening effects, defined by [Belarbi and Hsu \(1994\)](#). Details on these behavioral features and parameters are provided in the thesis by [Ulugtekin \(2010\)](#). The implemented uniaxial constitutive stress-strain relationship for reinforcing steel is the well-known nonlinear hysteretic model of [Menegotto and Pinto \(1973\)](#), extended by [Filippou et al. \(1983\)](#) to include isotropic strain hardening effects [Fig. 2(b)].

Experimental Program

Experimental results were obtained for five approximately third-scale wall specimens tested by [Tran and Wallace \(2012\)](#). The primary test variables included wall aspect ratio (1.5 and 2.0), axial load level ($0.025A_g f'_c$ and $0.10A_g f'_c$), and average shear stress level at nominal flexural capacity (between approximately 0.33 and $0.66\sqrt{f'_c}$ MPa or 4 and $8\sqrt{f'_c}$ psi). An overview of specimen properties, material characteristics, test setup, and instrumentation is presented in the following paragraphs, whereas detailed information can be found in [Tran \(2012\)](#).

The five cantilever wall specimens were 150 mm thick and 1,220 mm long, with lateral load applied at either 1,830 or 2,440 mm above the wall-foundation block interface. An axial load level of $0.10A_g f'_c$ was applied on the first four specimens and $0.025A_g f'_c$ on the fifth, where A_g is the cross-sectional area of the wall and f'_c is the specified concrete compressive strength. The wall horizontal and vertical web reinforcement ratios exceeded the ACI 318-11 code-specified minimum value of 0.0025 ([ACI 2011](#)). The minimum and maximum vertical boundary reinforcement ratios of the specimens were 3.2% and 7.1%, respectively. The specimens were designed to yield in flexure at a lateral load equal to approximately 80–90% of the nominal shear strength, under moderate and high shear demand levels. A representative wall cross section is illustrated in Fig. 3, whereas relevant parameters for all five specimens are presented in Table 1. Specimen names listed in Table 1 are descriptive of the wall specimen characteristics; for example, RW-A20-P10-S38 corresponds to a rectangular wall specimen (RW) with an aspect ratio of 2.0 (A20), axial load level equal to 10% of wall axial capacity (A10), and average shear stress level at nominal flexural capacity equal to $3.8\sqrt{f'_c}$ psi (S38) ($0.33\sqrt{f'_c}$ MPa).

Concrete with nominal compressive strength of 34.5 MPa was used for construction of all wall specimens. Boundary longitudinal reinforcement for each specimen consisted of eight A706 Grade 60 (nominal yield strength of 414 MPa) vertical bars, either #4 ($d_b = 12.70$ mm), #5 ($d_b = 15.87$ mm), or #6 ($d_b = 19.05$ mm), that were continuous over the wall height and incorporated heads at both ends. Vertical and horizontal web reinforcement for Tests 2, 4,

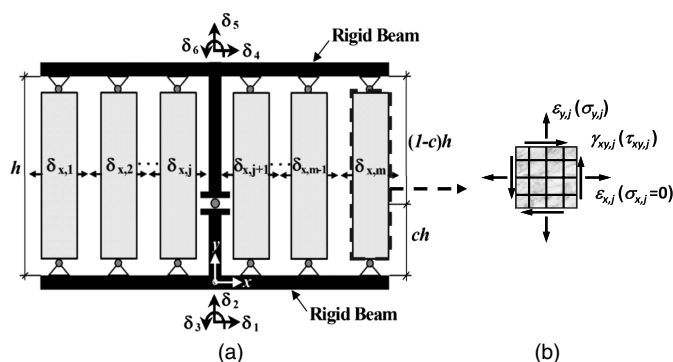


Fig. 1. SFI-MVLEM element

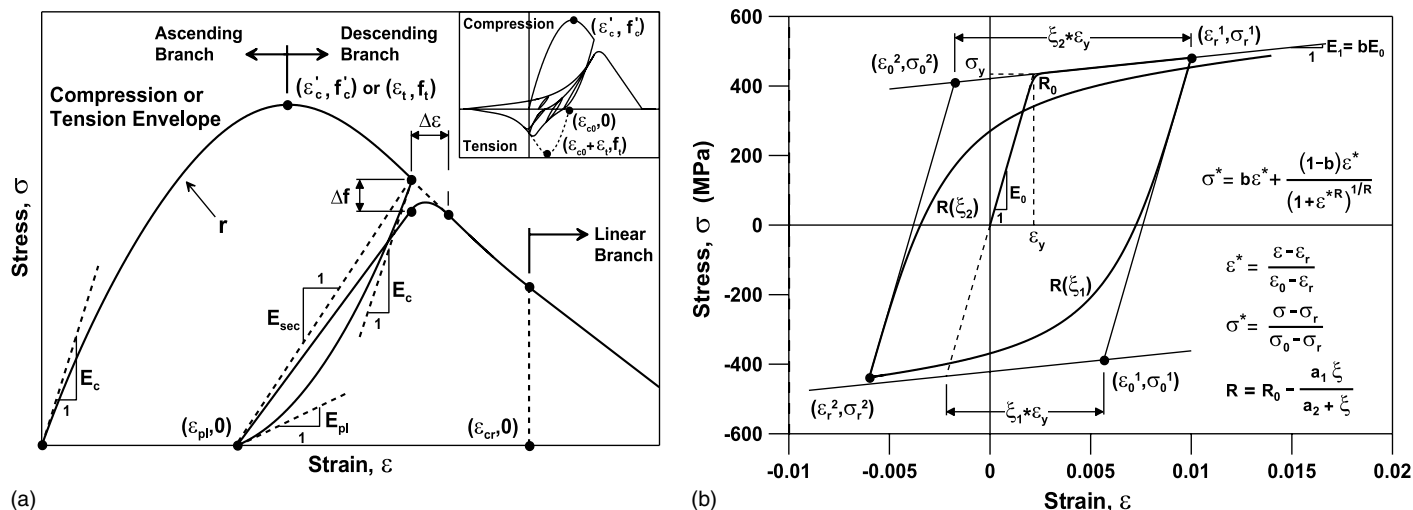


Fig. 2. Constitutive models for (a) concrete; (b) reinforcing steel

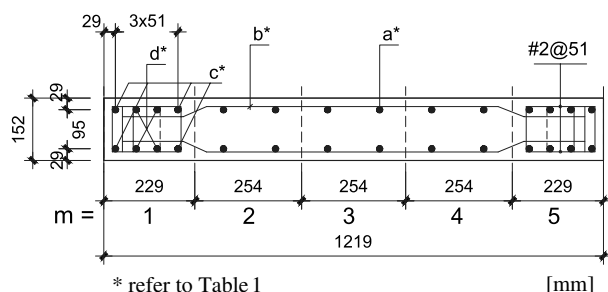


Fig. 3. Typical wall cross section with model discretization

and 5 were deformed #3 bars ($d_b = 9.52$ mm) of Grade 60 steel, whereas deformed D6 ($d_b = 6.00$ mm) web bars were used for Tests 1 and 3. Special boundary elements of the wall specimens were detailed based on a stress-based approach (ACI 318-11 Section 21.9.6; ACI 2011); smooth #2 bars ($d_b = 6.35$ mm) of Grade 40 steel were used as transverse reinforcement (hoops and crossties) in the boundary regions.

Reversed cyclic lateral loads were applied at the top of the specimens using a 890 kN-capacity hydraulic actuator while constant vertical (axial) loads were applied using two 1,000 kN-plunger cylinders; a schematic of the test setup is shown on Fig. 4. The testing protocol consisted of load-controlled and displacement-controlled cycles. Load-controlled cycles were performed generally at 1/8, 1/4, 1/2, and 3/4 of the expected yield force, after which the loading protocol was switched to displacement-controlled cycles, typically to drift ratios of 0.5, 0.75, 1.0, 1.5, 2.0, 3.0, and 4.0% (for Test 3 only) throughout the remainder of each test.

Wall specimens were heavily instrumented to obtain detailed deformation measurements. Linear variable differential transducers (LVDTs) were used to measure wall foundation sliding and uplift, lateral displacements at various height levels, flexural, shear, and sliding shear deformation components, and average concrete strains over various gauge lengths. Fig. 5 shows the typical configuration of LVDTs (on both sides of the specimens) used for Tests 1 through 5. By processing the deformations measured by the LVDTs mounted in vertical, horizontal (front side, Fig. 5), and "X" configurations (back side, Fig. 5), wall lateral displacements measured at the top and story levels were separated into flexural and shear deformation components using the methodology

described by Massone and Wallace (2004). Reinforcing steel strains were also measured at a total of 30 locations, using strain gauges affixed to the boundary longitudinal and transverse reinforcement and the vertical and horizontal web reinforcement, over a height of approximately half the length of each wall ($l_w/2$) from the wall–foundation block interface.

Calibration of the Analytical Model

Geometry

The analytical models created for all of the wall specimens were discretized along the wall length using five RC panel elements ($m = 5$), where the two outer panel elements (macrofibers) represent the confined wall boundaries and the remaining three represent the wall web (Fig. 3). Discretization of the wall specimens along the wall height was performed considering the locations of the instrumentation used to measure deformations on the wall specimens (e.g., LVDTs, Fig. 5), to allow consistent deformation comparisons between model predictions and experimental results. Accordingly, six SFI-MVLEM elements ($n = 6$) were used along the height of wall specimens with aspect ratio of 2.0 (Tests 1 and 2), and five SFI-MVLEM elements ($n = 5$) were used along the height of specimens with aspect ratio of 1.5 (Tests 3, 4, and 5), as shown in Fig. 5. As reported by Tran and Wallace (2012), during the tests, inelastic deformations on the walls were observed along a height approximately equal to half the wall length from the base (i.e., $l_w/2 = 610$ mm). In the analytical model, this region was represented using two SFI-MVLEM elements for all specimens (Fig. 5). A value of 0.4 was selected for the parameter c defining the center of relative rotation for each wall element, based on previous recommendations by Vulcano et al. (1988) and Orakcal and Wallace (2006).

Materials

The reinforcing steel stress-strain relationship described by the Menegotto and Pinto (1973) model was calibrated to reasonably represent the experimentally obtained properties of the reinforcing bars used in tests. The tensile yield strength and strain-hardening parameters were modified according to empirical relations proposed by Belarbi and Hsu (1994) to include the effect of tension stiffening on steel bars embedded in concrete. Fig. 6 shows the

Table 1. Properties of Wall Specimens

Test number	Specimen code	h_w/l_w	$P_{ax}/A_g f'_c$		$\rho_l = \rho_l$ (%)	Web reinforcement		Boundary reinforcement		$V@M_n/V_n$		$V@M_n/A_{cv}\sqrt{f'_c}$	
			design	actual		a^{*a}	b^{*a}	ρ_b (%)	c^{*a}	design	actual	design	actual
1	RW-A20-P10-S38	2.0	0.10	0.073	0.27	6D6a @ 140 mm	D6b @ 140 mm	3.23	4#4	0.80	0.81	3.8	3.6
2	RW-A20-P10-S63	2.0	0.10	0.073	0.61	5#3 @ 152 mm	#3 @ 152 mm	7.11	4#6	0.88	0.91	6.3	6.1
3	RW-A15-P10-S51	1.5	0.10	0.077	0.32	7D6a @ 114 mm	D6b @ 114 mm	3.23	4#4	0.80	0.83	5.1	4.9
4	RW-A15-P10-S78	1.5	0.10	0.064	0.73	6#3 @ 127 mm	#3 @ 127 mm	6.06	4#5	0.84	0.85	7.8	7.0
5	RW-A15-P2.5-S64	1.5	0.025	0.016	0.61	5#3 @ 152 mm	#3 @ 152 mm	6.06	4#6	0.79	0.79	6.4	5.8

^aRefer to Fig. 3.

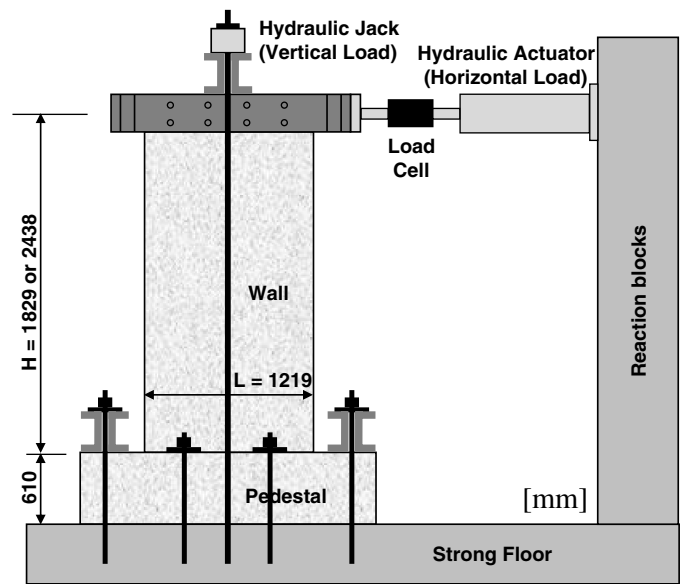


Fig. 4. Scheme of test setup

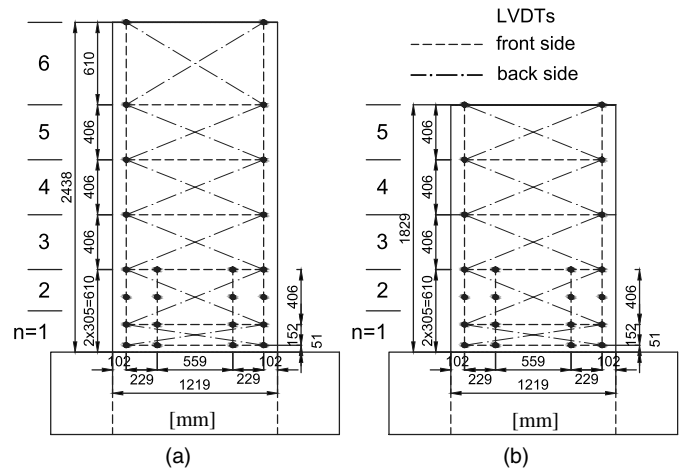


Fig. 5. LVDT sensor configuration for (a) Tests 1 and 2; (b) Tests 3, 4, and 5

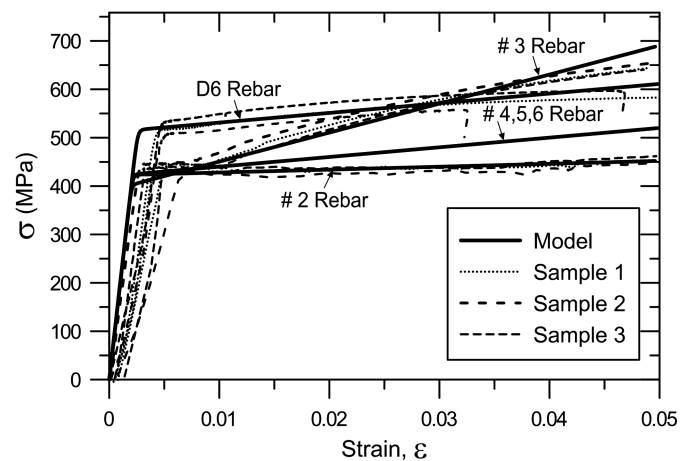


Fig. 6. Calibration of steel constitutive model

Table 2. Calibrated Constitutive Parameters for Reinforcing Steel

Parameter	Reinforcement bar					
	D6a	#2	#3	#4	#5	#6
f_y (MPa)	450.2	423.4	443.3	472.7	474.6	477.2
E_0 (MPa $\times 10^5$)	2.0	2.0	2.0	2.0	2.0	2.0
b	0.02	0.003	0.02	0.01	0.01	0.01

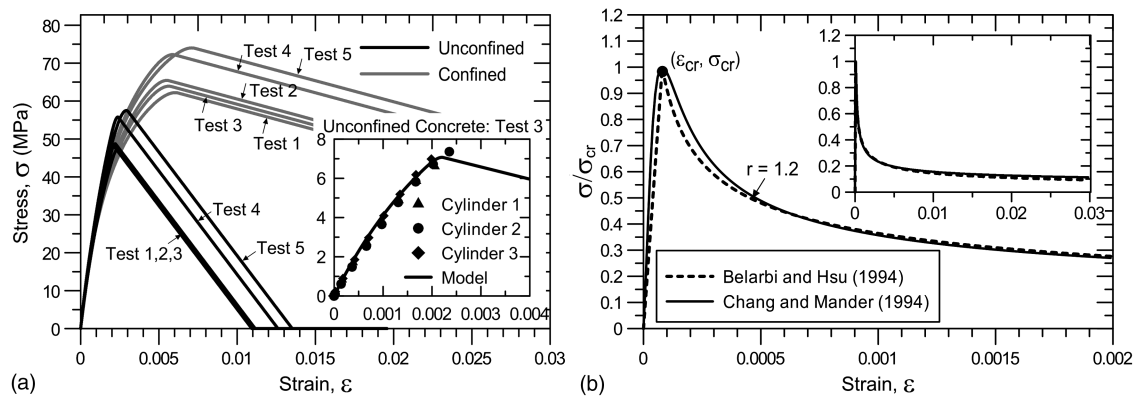
calibrated steel stress-strain relationships in tension along with the stress-strain relationships obtained experimentally for bare reinforcing bar coupons of D6 ($d_b = 6.00$ mm), #2 ($d_b = 6.35$ mm), and #3 ($d_b = 9.52$ mm) bars. Monotonic parameters used for the calibration of the steel stress-strain relationship in tension are listed in Table 2. The parameters describing the cyclic stiffness degradation characteristics of the reinforcing bars were calibrated as $R_0 = 20$, $a_1 = 18.5$, and $a_2 = 0.15$, as proposed originally by Menegotto and Pinto (1973).

The monotonic envelope of the stress-strain model for unconfined concrete in compression was calibrated using monotonic test results conducted (on wall test dates) on standard 150×300 mm concrete cylinders by matching the analytical and experimental values of compressive strength f'_c , the strain at compressive strength ϵ'_c , initial tangent modulus E_c , and the parameter r defining the shape of the monotonic stress-strain curve. The stress-strain envelopes for confined concrete in compression were obtained by computing the peak stress of confined concrete (f'_{cc}) and the strain at peak stress (ϵ'_{cc}) based on the area, configuration, spacing, and yield stress of the transverse reinforcement, using the confinement model by Mander et al. (1988), whereas the initial tangent modulus for confined concrete (E_{cc}) and corresponding shape parameter (r_c)

are obtained based on the peak stress of confined concrete (f'_{cc}) using empirical relations proposed by Chang and Mander (1994); see also Orakcal and Wallace (2006). The postpeak slope of the monotonic stress-strain envelopes for both confined and unconfined concrete were calibrated via the parameter ϵ_{cr} to agree with the postpeak slope of the Saatcioglu and Razvi (1992) model, yielding the results shown in Fig. 7(a). The parameters used for calibrating the stress-strain envelopes for unconfined and confined concrete in compression are presented in Table 3.

The tensile strength of concrete was determined from the relationship $f_t = 0.31 \sqrt{f'_c}$ (MPa), and a value of 0.00008 was selected for the strain at the peak monotonic tensile stress ϵ_t , as suggested by Belarbi and Hsu (1994). The shape of the monotonic tension envelope of the Chang and Mander (1994) model was calibrated via the parameter r to reasonably represent the average post-crack stress-strain relation proposed by Belarbi and Hsu (1994), which represents tension stiffening effects on concrete [Fig. 7(b)]. The parameters used for calibrating the stress-strain model for concrete in tension are also presented in Table 3. Biaxial material parameters representing compression softening and hysteretic damage of concrete in compression were calibrated per the original empirical relationships proposed by Vecchio and Collins (1993) and Mansour et al. (2002), respectively.

Regarding the shear-resisting mechanism along cracks, as discussed in the companion paper (Koložvari et al. 2014), model predictions for the overall lateral load-displacement response and the contributions of shear and flexural deformations to lateral displacement are not very sensitive to the shear friction coefficient η , whereas such response predictions were observed to be modestly sensitive with respect to selection of the dowel action stiffness parameter α . For example, analytical predictions obtained for

**Fig. 7.** Calibration of concrete constitutive model: (a) compression; (b) tension**Table 3.** Calibrated Constitutive Parameters for Concrete in Compression and Tension

Material	Parameter	RW-A20-P10-S38		RW-A20-P10-S63		RW-A15-P10-S51		RW-A15-P10-S78		RW-A15-P2.5-S64	
		Boundary (confined)	Web (unconfined)	Boundary (confined)	Web (unconfined)	Boundary (confined)	Web (unconfined)	Boundary (confined)	Web (unconfined)	Boundary (confined)	Web (unconfined)
Concrete in compression	f'_c (MPa)	62.2	47.1	65.4	48.6	63.9	48.7	72.2	55.8	74.0	57.5
	ϵ'_c	0.006	0.002317	0.0055	0.002014	0.0056	0.002202	0.0059	0.002371	0.0071	0.002912
	E_c (MPa)	38,810	34,963	39,555	35,377	39,203	35,418	41,051	37,252	41,423	37,680
	ϵ_{cr}	0.062	0.0111	0.063	0.0112	0.062	0.0113	0.071	0.0126	0.074	0.0135
	R	10.2	20	10.8	20	10.5	20	12.2	15	12.4	9
Concrete in tension	f_t (MPa)	2.13		2.16		2.16		2.31		2.35	
	ϵ_t	0.00008		0.00008		0.00008		0.00008		0.00008	
	E_c (MPa)	34,963		35,377		35,418		37,252		37,679	
	ϵ_{cr}	∞		∞		∞		∞		∞	
	R	1.2		1.2		1.2		1.2		1.2	

Table 4. Calibrated Values of Parameter α

Test number	Specimen code	Parameter α
1	RW-A20-P10-S38	0.020
2	RW-A20-P10-S63	0.005
3	RW-A15-P10-S51	0.010
4	RW-A15-P10-S78	0.005
5	RW-A15-P2.5-S64	0.001

specimen RW-A15-P10-S78 (Test 4; Tran and Wallace 2012) showed that doubling the value of parameter α from 0.005 to 0.01 decreases the contribution of shear deformations from approximately 48–43% (by approximately 15%). In addition, model predictions obtained for the lateral load versus top displacement response of the walls are sensitive to the value selected for parameter α primarily within the pinching region of the response, whereas predictions for the lateral stiffness, lateral load capacity, and lateral deformation capacity characteristics of the walls are not significantly influenced. Nevertheless, model calibration studies were conducted by comparing the experimentally measured lateral-load versus wall-top-displacement responses with analytical predictions obtained using a constant shear friction coefficient of $\eta = 1.0$ (commonly adopted by other researchers; e.g., Wood 1990; Valluvan et al. 1999; Chorzepa et al. 2011) and varying dowel action stiffness parameter α (values of $\alpha = 0.001, 0.002, 0.005, 0.01$, and 0.02 were considered) to optimize the correlation between model and test results for each specimen; the criterion for calibration of parameter α was minimizing the difference between test results and model predictions in terms of the cumulative area under the hysteretic lateral load-displacement loops. Calibrated values obtained for parameter α are presented in Table 4.

As shown in Table 4, the value of parameter α that yields the most accurate predictions of experimentally measured response varies for the five specimens, suggesting that the selection of parameter α for obtaining optimum accuracy would benefit from additional studies. Future studies could concentrate on developing a method (or an equation) to improve the selection of the parameter α , by comparing model results with experimental studies available in the literature on a broader range of wall specimens with different geometries and reinforcement characteristics than considered here. Alternatively, implementation of a more robust constitutive model for dowel action that might avoid the need for this calibration could be considered.

Analytical Results and Comparison with Test Results

The calibrated shear-flexure interaction model (SFI-MVLEM) described in the companion paper (Koložvari et al. 2014) was implemented in *Matlab* (MathWorks 2004) to predict the response of the five moderate-aspect-ratio wall specimens tested by Tran and Wallace (2012). A displacement-controlled nonlinear analysis strategy, with prescribed lateral displacement histories applied at the top of the walls, was selected to correlate the model predictions with results of the force/drift-controlled cyclic tests. The axial load applied at the top of each wall model corresponds to the average result of the actual forces applied by the vertical cylinders mounted at the top of each wall specimen (Table 1). Test results were compared to model predictions in terms of lateral load versus top displacement responses, contributions of flexural and shear deformations to wall lateral displacements and their distribution along the wall height, vertical growth of the walls that is due to yielding of longitudinal reinforcement, average vertical concrete strains, plastic

hinge rotations, and concrete crack patterns. Only selected comparisons are presented in the following paragraphs, whereas response comparisons for all specimens are available in the Ph.D. dissertation by Koložvari (2013).

Figs. 8(a–e) compare the experimentally measured and analytically predicted lateral load versus top displacement responses for Tests 1–5 and average contributions (average of positive and negative loading cycles) of shear deformations to wall top displacement at selected lateral drift levels. Average contributions (average of all drift levels) of shear deformations to top displacement for all five wall specimens are compared in Fig. 8(f). It can be observed from Figs. 8(a–e) that the analytical model captures reasonably well the lateral load capacity and stiffness characteristics of all specimens for most of the applied drift levels. Lateral loads on the specimens are generally overestimated at drift levels lower than 0.5%, indicating a moderate overprediction of lateral stiffness, whereas for drift levels between 0.5 and 2.0%, analytically predicted lateral load capacities are within the $\pm 10\%$ range of the experimentally measured capacities. In addition, cyclic characteristics of the response, including stiffness degradation, plastic (residual) displacements, and pinching behavior (moderate pinching in Tests 1–4 for specimens with axial load of $0.10A_g f'_c$ and pronounced pinching in Test 5 for the specimen with axial load of $0.025A_g f'_c$) are well represented in the model results for all wall specimens.

Significant strength degradation occurred at a drift level of 3.0% for Tests 1, 2, 4, and 5 and at 4.0% drift for Test 3. During Test 1 (RW-A20-P10-S38) and Test 3 (RW-A15-P10-S51), strength degradation was initiated by crushing of core concrete and buckling of longitudinal reinforcement at the wall boundaries, followed by progressive degradation associated with diagonal tension failure along two major diagonal cracks. During Test 2 (RW-A20-P10-S63), strength loss was caused by crushing of concrete at the wall boundary, along with crushing along diagonal compression struts near the wall base, leading to out-of-plane buckling of longitudinal boundary reinforcement. During Test 4 (RW-A15-P10-S78) and Test 5 (RW-A15-P2.5-S64), strength degradation was caused by crushing of diagonal compression strut at the wall base, resulting in progressive degradation associated with lateral instability of the wall boundary region (out-of-plane buckling) and sliding shear adjacent to the wall-foundation interface of the wall for Test 4 and in-plane buckling of longitudinal boundary reinforcement together with significant sliding shear failure for Test 5 (Tran 2012). Although the analytical model captures the initiation of strength degradation in the concrete stress-strain behavior within the boundary elements, the significant strength loss observed in some of the tests is not represented in the analysis results because of the inability of the model to simulate failure mechanisms associated with buckling or fracture of reinforcing bars or sliding shear failure near the base of the walls. Therefore, for the loading cycles applied on the specimens to ultimate lateral drift levels, the analytical model tends to generally overestimate their lateral load/drift capacity.

Figs. 8(a–e) also compare the experimentally measured and analytically predicted average (of positive and negative loading cycles) contributions of shear deformations to the lateral top displacement of the wall specimens at drifts levels of 0.5, 0.75, 1.0, 2.0, and 3.0%; more detailed comparisons are presented in the Ph.D. dissertation by Koložvari (2013). Comparisons presented in Fig. 8 reveal that the analytical model predicts, with reasonable accuracy, the experimentally measured shear deformation contributions for the five wall specimens. For Test 1 (RW-A20-P10-S38), the analytical model underestimates shear deformation contributions at drift levels lower than 1.5% by approximately 10%, whereas for the remaining drift levels, model predictions are in good agreement with experimental results. The analytically predicted average

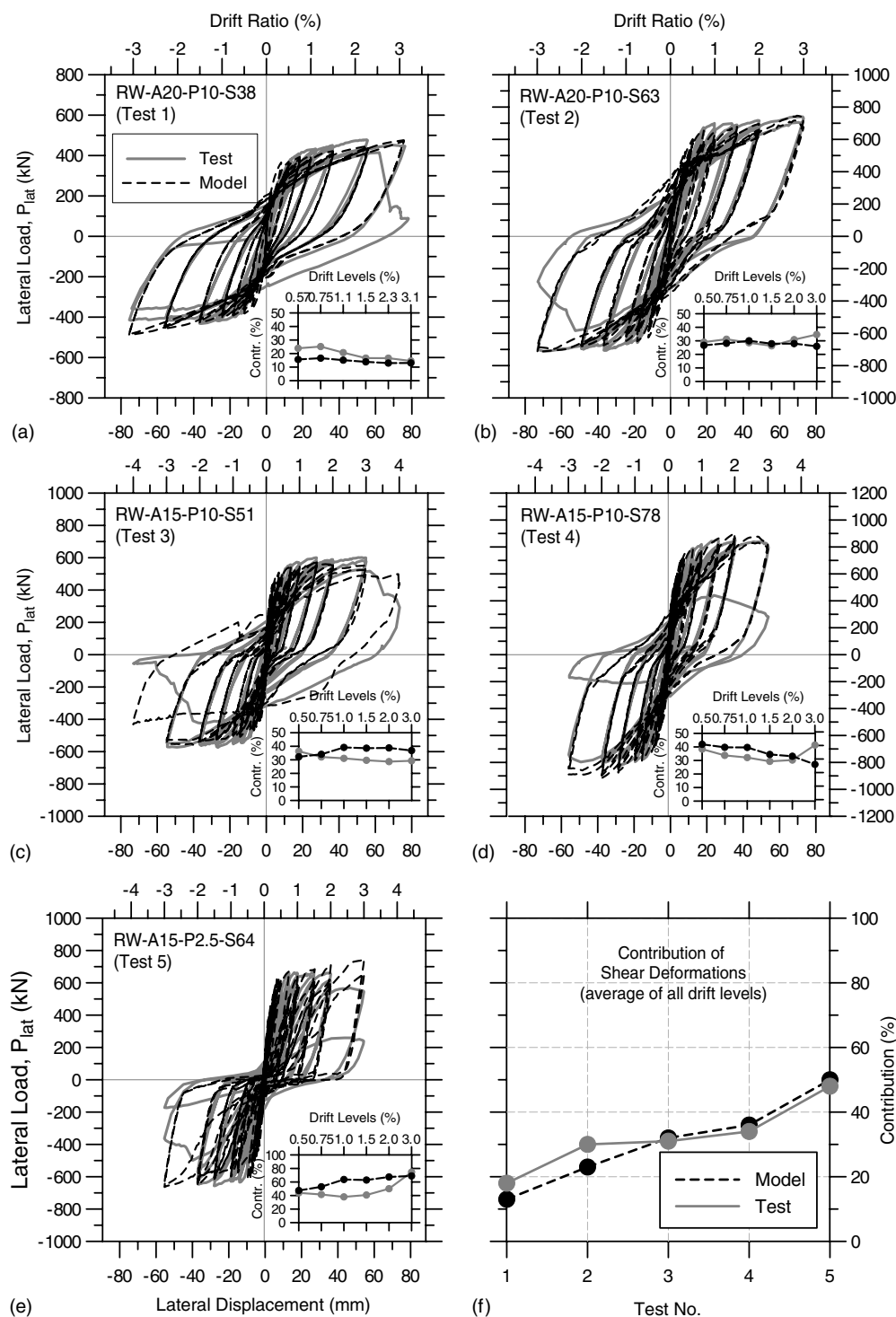


Fig. 8. Lateral load versus wall top displacement responses for (a) Test 1; (b) Test 2; (c) Test 3; (d) Test 4; (e) Test 5; (f) average contributions of shear deformations for Tests 1–5

contributions of shear deformations for Test 2 (RW-A20-P10-S63) and Test 4 (RW-A15-P10-S78) (i.e., for specimens with high shear stress demand at flexural capacity) are also in agreement with experimental results; model predictions are falling within $\pm 5\%$ of experimental measurements for almost all drift levels, except for 3.0% drift where significant degradation in lateral strength occurred. For Test 3 (RW-A15-P10-S51), the model overestimates the experimental results by approximately 10% at drift levels larger than 0.75%, whereas for Test 5 (RW-A15-P2.5-S64), model predictions are larger than test measurements by approximately 20% between

drift levels of 0.75 and 2.0%. Furthermore, Fig. 8(f) reveals that the experimentally obtained average (of all applied drift levels) contributions of shear deformations to top displacement generally increase with an increase of wall shear stress demand and a decrease of wall aspect ratio and axial load level (Table 1). As shown on Fig. 8(f), the analytical model captures well the systematic tendencies of shear deformations in five specimens by replicating the observed trend of the average contribution of shear deformations with respect to wall shear demand, aspect ratio, and axial load with results that overestimate shear contributions by approximately

15–20% for Test 1 (RW-A20-P10-S38) and Test 2 (RW-A20-P10-S63) and underestimate shear contributions by less than 5% for Test 3 (RW-A15-P10-S51), Test 4 (RW-A15-P10-S78), and Test 5 (RW-A15-P2.5-S64).

Comparisons of the experimentally measured and analytically predicted flexural and shear deformation components of the lateral load versus top displacement response for Test 2 (RW-A20-P10-S63, aspect ratio 2.0 and high shear stress demand at flexural capacity) and Test 3 (RW-A15-P10-S51, aspect ratio 1.5 and moderate shear stress demand) are presented in Figs. 9 and 10, respectively. It can be observed from the figures that the analytical model successfully captures the nonlinear flexural and shear deformations and their coupling throughout the entire cyclic loading history. As revealed in both experimental and analytical results, flexural and shear yielding occur almost simultaneously for both wall specimens at a lateral load level of approximately 700 and 600 kN for Test 2 and Test 3, respectively. As well, the model successfully reproduces the shapes of the flexural and shear load versus displacement responses, with flexural response characterized by no

pinching or low-level pinching and shear behavior characterized by a highly pinched load-deformation response. Whereas the analytical model captures the flexural stiffness of the wall at all drift levels, shear stiffness is overestimated at drift levels lower than 0.5%. The magnitudes of nonlinear flexural and shear deformation components predicted by the model generally match the experimentally measured values throughout the cyclic loading history. However, as depicted in Fig. 9(b), the analytical model underestimates the shear deformations measured during Test 2 for the second loading cycle to 3.0% drift in the negative direction because of its inability to capture the lateral instability of the boundary zone observed during the test, which caused progressively greater lateral strength degradation.

Comparisons of measured and predicted flexural and shear displacement profiles (along the height of the wall) for Test 1 (RW-A20-P10-S38) are shown in Fig. 11. For both experimental and analytical results, displacement profiles were generated at peak top displacements during the first loading cycle to lateral drift levels of 0.5, 0.75, 1.0, and 2.0%, in positive and negative loading

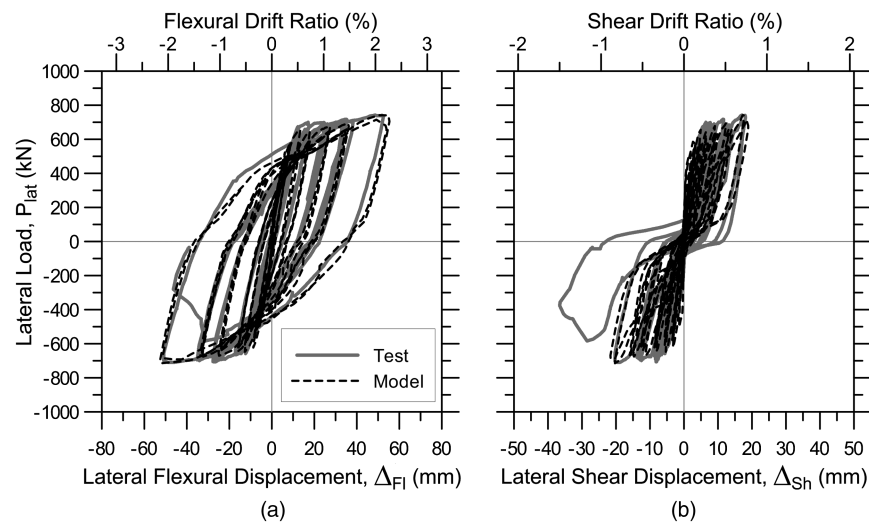


Fig. 9. Load-displacement response for Test 2: (a) flexure; (b) shear

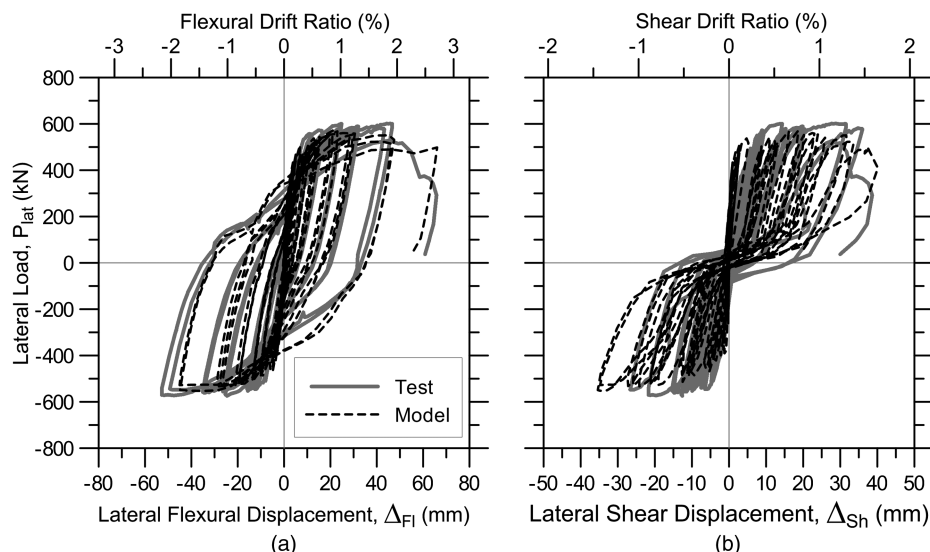


Fig. 10. Load-displacement response for Test 3: (a) flexure; (b) shear

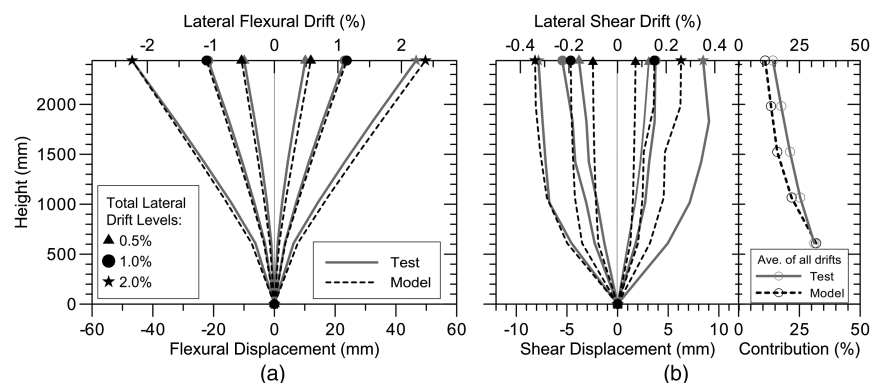


Fig. 11. Displacement profiles for Test 1: (a) flexure; (b) shear

directions, at heights of 610, 1,000, 1,420, and 1,830 mm measured from the base of the wall. It can be observed from Fig. 11(a) that in both experimental and analytical results, nonlinear flexural deformations (rotations) develop mostly within the bottom region of the wall, along a height of 610 mm ($l_w/2$, a commonly used plastic hinge length for walls with well-detailed boundaries), whereas the flexural displacement profiles are almost linear above this height, indicating that flexural deformations are relatively small in the upper regions of the wall. The analytical flexural displacement profiles reveal that the model successfully captures the plastic hinge length of the wall and the distribution of flexural deformations along the height of the wall. As well, the magnitudes of flexural displacements along wall height are well predicted by the analytical model, with approximately 5% deviation between model and test results.

The comparisons shown in Fig. 11(b) indicate that the shape of the measured and predicted shear deformation profiles agree reasonably well, demonstrating that the model captures the experimentally observed concentration of shear deformations along the bottom region of the wall. The largest shear distortions were obtained over a wall height of $l_w/2$ (610 mm), as was noted for nonlinear flexural deformations. The analytical model is capable of predicting nonlinear shear deformations even for a wall that yields in flexure, which has been observed in the current and previously conducted experimental studies (e.g., Tran and Wallace 2012; Massone and Wallace 2004; Oesterle et al. 1976, 1979). The model reasonably predicts the magnitude of shear displacements along wall height at low and moderate drift levels, whereas for this specimen (Test 1, RW-A20-P10-S38), analytical results tend to underestimate the experimentally measured shear displacements at a drift level of 2.0%, albeit for loading in the positive direction only. Fig. 11(b) further reveals that the average (of all drift levels) contribution of shear deformations distributed over the height of the wall is predicted by the analytical model with reasonable accuracy (generally underestimated by 5%). In both experimental and analytical results, shear deformations contribute to lateral displacements by approximately 35% at the height of $l_w/2$ (610 mm) from the wall base and 10–15% at the top of the wall.

Comparison of test measurements and analytical predictions for the vertical growth versus lateral displacement relationship obtained for Test 4 (RW-A15-P10-S78, subjected to the design axial load of $0.10A_g f'_c$) are presented in Fig. 12. It can be observed from the figure that the analytical model is capable of capturing the vertical growth of the wall specimen (vertical displacement at the top of the wall) associated with yielding of longitudinal reinforcement and migration of the neutral axis. Vertical growth of the wall is predicted reasonably well throughout most of the cyclic loading history, and model predictions are in overall agreement with the test measurements in terms of both the maximum vertical growth

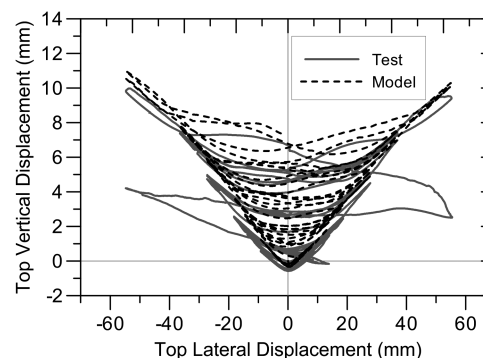


Fig. 12. Vertical growth versus top lateral displacement relation for Test 4

magnitudes at peak lateral displacement values and the residual vertical growth magnitudes at zero lateral displacement. The vertical growth of this specimen was reversed (decreased) during the second loading cycle to the ultimate drift ratio of 3.0% because of substantial in-plane buckling of longitudinal reinforcement at both wall boundaries, which is not represented in the model results.

Fig. 13(a) compares measured and predicted vertical strain profiles (along the wall length) at the bottom of the wall specimen for selected peak drift levels applied during Test 4 (RW-A15-P10-S78), whereas vertical strains at a single wall boundary at various peak drift levels are compared in Fig. 13(b). The experimentally measured average vertical concrete strains shown in Fig. 13(a) are obtained from measurements of vertical LVDTs located at 100, 330, 890, and 1,120 mm along the length of the wall specimens, over a gauge length of 356 mm (from 50 to 406 mm from the wall base), whereas the average strains at the wall boundary plotted in Fig. 13(b) are obtained at 100 mm from the boundary of the wall, over a gauge length of $l_w/2$ (610 mm) from the wall base. In the analytical results, vertical strain profiles plotted in Fig. 13(a) are obtained from the average strains in the bottom-most SFI-MVLEM element of 305 mm height, whereas peak strains at the wall boundary shown in Fig. 13(b) are obtained from the bottom two SFI-MVLEM elements, over a total height of 610 mm.

Results shown in Fig. 13(a) illustrate that the experimentally measured vertical strain profiles are almost linear for drift levels of 0.5 and 1.0%. At a drift level of 2.0%, the experimentally measured vertical strain profile is characterized by strain relaxation in the wall boundary in tension, resulting in a nonlinear strain profile, which cannot be captured analytically because of the assumption in the model that plane sections remain plane. Otherwise, the analytical model adequately reproduces the experimentally measured

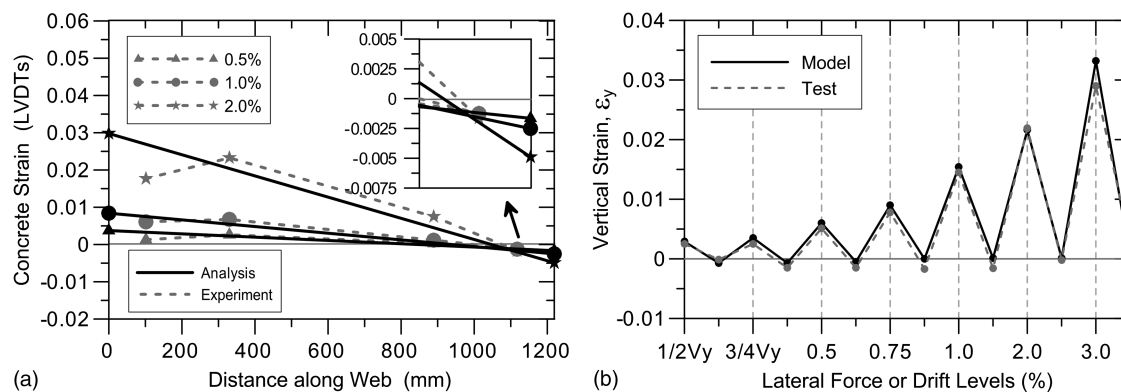


Fig. 13. Average vertical strains for Test 4: (a) strain profiles; (b) strain histories

strain profiles and provides reasonably good predictions for the vertical strains in both tension and compression regions and the location of the neutral axis. Orakcal and Wallace (2006) have discussed that using an analytical model that does not account for coupling of flexural and shear responses may lead to underestimation of vertical compressive strains in a wall because such a model is incapable of considering the influence of shear deformations on flexural deformations (i.e., vertical strains). Results presented in Fig. 13(a) reveal that the shear-flexure interaction model (SFI-MVLEM) used in this study shows potential for reasonably accurate predictions of compressive strain. Detailed information on comparisons of analytical predictions obtained using an “uncoupled” wall model (e.g., the displacement-based fiber model implemented in OpenSees; McKenna et al. 2000) and the proposed SFI-MVLEM are presented in the Ph.D. dissertation by Kolozvari (2013).

For evaluating the average vertical strain predictions of the analytical model over a larger wall height (plastic hinge length, $l_w/2$), measured and predicted vertical strains at a single wall boundary at various peak drift levels are compared in Fig. 13(b). It can be observed from the figure that the analytical model reasonably captures the average tensile strains at the wall boundary for most of the peak drift levels applied throughout the loading history. Tensile strains at the boundary (corresponding to loading cycles in the positive direction) are generally overestimated by no more than 5% at all drift levels except 3.0%. Compressive strain predictions of the model are not as accurate as shown in Fig. 13(a), possibly because measurements over larger gauge lengths typically impair the reliability of experimentally obtained concrete compressive strains. The analytical model is capable of capturing the vertical growth of the wall boundary after yielding of the boundary longitudinal reinforcement; in both experimental and model results, average compressive strains tend to decrease at large peak drift levels. In the experimental results, this vertical growth is pronounced at drift levels larger than 1.5%, whereas in the analytical results a constant rate of growth can be observed at drift levels larger than 0.5%.

Fig. 14 compares experimentally measured and analytically predicted rotations, at peak drift levels, over the assumed plastic hinge length of $l_w/2$ (610 mm) for Test 3. The experimental rotations are obtained using data from two LVDTs mounted on each side of the wall, measuring the vertical deformations over a gauge length of 610 mm from the wall base. Results presented in Fig. 14 reveal that the measured and predicted rotations are in good agreement (within $\pm 10\%$) for all drift levels, indicating that the model accurately reproduces the nonlinear flexural deformations developing over the plastic hinge region of the wall.

In Fig. 15, the experimentally observed crack pattern on the wall recorded during Test 5 at a drift ratio of 2.0% (gray lines) is

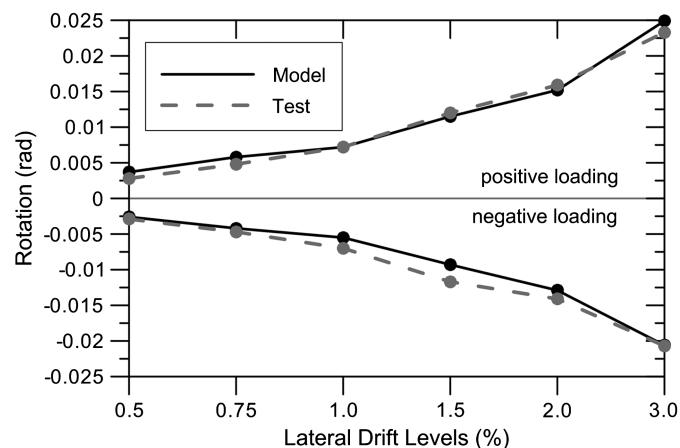


Fig. 14. Plastic hinge rotations for Test 3

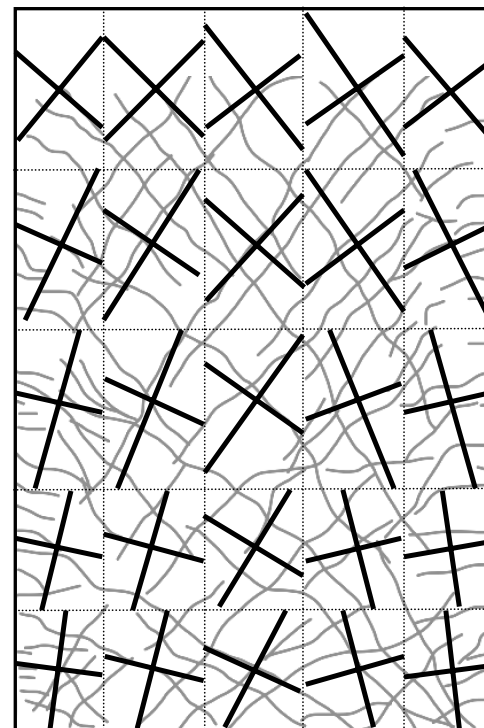


Fig. 15. Experimental (gray) and analytical (black) cracking patterns for Test 5 at 2.0% drift

compared with the crack orientations predicted by the analytical model (black lines). The predictions of the analytical model for the orientation and distribution of cracks on the wall are in reasonable agreement with the observed crack pattern, suggesting that the cracking criteria (rotating principal strain and stress directions prior to cracking; a crack develops when principal tensile strain reaches the monotonic cracking strain of concrete) and the orthogonal crack assumption of the model are both reasonable. The orientation of the cracks is more horizontal at the wall boundaries where flexural (vertical) strains predominate over shear strains, whereas the cracks are more inclined toward the middle of the wall web where shear (diagonal tension) strains are more dominant. As well, because flexural effects decrease along the wall height, orientation of the cracks at wall boundaries becomes more inclined toward the top of the wall.

Summary and Conclusions

The intent of this paper was to convey detailed information on calibration and experimental validation of an analytical model described in the companion paper (SFI-MVLEM; Kolozvari et al. 2014) that integrates shear-flexure interaction in RC walls subjected to cyclic loading conditions. The model incorporates constitutive RC panel behavior, described by a fixed-strut-angle modeling approach, into a two-dimensional fiber-based model. Analytical model responses were compared against experimental results obtained for five moderately slender RC wall specimens that experienced nonlinear shear deformations and significant levels of shear-flexure interaction (Tran and Wallace 2012). The robust constitutive relationships implemented into the SFI-MVLEM for concrete and reinforcing steel were calibrated based on the as-tested properties of the materials used in the construction of the walls modeled and by parameters validated previously by other researchers (e.g., for confinement, tension stiffening, compression softening, biaxial damage, and hysteretic behavior). Test measurements were processed to allow consistent comparisons between experimental and analytical results at various response levels and locations (e.g., story displacements, shear and flexural deformation components, plastic hinge rotations, and average strain profiles).

Overall, the SFI-MVLEM is shown to be an effective modeling approach for response prediction of moderately slender RC walls in which shear-flexure interaction behavior is significant. The model captures the experimentally observed coupling between nonlinear flexural and shear responses throughout the entire cyclic loading history. The model provides accurate predictions of the experimentally measured lateral load versus top displacement responses, including wall lateral load capacity and stiffness at varying drift levels and cyclic (stiffness degradation and pinching) characteristics of the load-displacement response. In addition, relative contributions of flexural and shear deformations to wall lateral displacements and their distribution over the wall height are all predicted by the analytical model with reasonable accuracy. On the local response level, the model provides good predictions for the average vertical strains on a wall, both compressive and tensile, and average rotations over the region of inelastic deformations ($l_w/2$).

Two major model shortcomings were identified. Only limited calibration studies were conducted for the model parameters used to represent a shear-resisting mechanism across cracks (five test specimens); therefore, additional studies are needed on a broader data set to confirm and refine the values determined here (e.g., for walls without special boundary elements). As well, the strength degradation observed in the five test walls used in this study was not represented in the analysis results because of the inability of the

model to simulate the experimentally observed failure mechanisms, including buckling of reinforcing bars, lateral instability of the boundary zone, and sliding shear near the wall base.

Future studies could focus on extensive calibration of the parameters describing the contribution of dowel action and shear aggregate interlock effects to the shear transfer mechanism across cracks, using a large number of test results available in the literature on a broader range of wall specimens with different geometries, reinforcement characteristics, and axial load levels, and on development and implementation of more robust constitutive models to represent shear resisting mechanisms along the cracks. Future studies could also concentrate on development and implementation of rebar buckling and fracture behavior into the constitutive relationship for reinforcing steel and on constitutive modeling of the sliding shear mechanism above the base of a wall, which would enable the analytical model to capture wall failure modes associated with these mechanisms.

Acknowledgments

The work presented in this paper was supported by funds from the National Science Foundation under Grants CMMI-0825347 and CMMI-1208192. The test results used in this study were obtained from experimental studies performed in a laboratory renovated with funds provided by the National Science Foundation under Grant No. 0963183, which is an award funded under the American Recovery and Reinvestment Act of 2009 (ARRA). The assistance of Dr. A. Salamanca and Senior Development Engineer S. Keowen are greatly appreciated. Laboratory assistants C. Hilson, B. Gerlick, R. Marapao, K. Weiland, S. Garcia, I. Wallace, L. Herrera, J. Diaz, F. Cifelli, K. Pham, and G. Schwartz also helped with specimen construction, test preparation, and test completion. Any opinions, findings, and conclusions expressed in this paper are those of the authors and do not necessarily reflect those of the supporting organizations or other people acknowledged herein.

References

- American Concrete Institute (ACI). (2011). *ACI 381-11*, Farmington Hill, MI.
- Barda, F., Hanson, J. M., and Corley, W. G. (1976). "Shear strength of low-rise walls with boundary elements." *Research and development Bulletin, RD043.01D*, Construction Technology Laboratories, Portland Cement Association, Washington, DC, 19.
- Belarbi, A., and Hsu, T. C. (1994). "Constitutive laws of concrete in tension and reinforcing bars stiffened by concrete." *ACI Struct. J.*, 91(4), 465–474.
- Beyer, K., Dazio, A., and Priestley, M. J. N. (2011). "Shear deformations of slender reinforced concrete walls under seismic loading." *ACI Struct. J.*, 108(2), 167–177.
- Chang, G. A., and Mander, J. B. (1994). "Seismic energy based fatigue damage analysis of bridge columns. Part I: Evaluation of seismic capacity." *NCEER Technical Rep. No. NCEER-94-0006*, State Univ. of New York, Buffalo, NY, 222.
- Chorzepa, M., Kim, Y. J., Yun, G. J., Harmon, G. T., and Dyke, S. (2011). "Cyclic shear-friction constitutive model for finite element analysis of reinforced concrete membrane elements." *ACI Struct. J.*, 108(3), 324–331.
- Filippou, F. C., Popov, E. G., and Bertero, V. V. (1983). "Effects of bond deterioration on hysteretic behavior of reinforced concrete joints." *EERC Rep. No. UCB/EERC-83/19*, Earthquake Engineering Research Center, Univ. of California, Berkeley, CA, 184.
- Fischinger, M., Rejec, K., and Isaković, T. (2012). "Modeling inelastic shear response of RC walls." *Proc., 15th World Conf. on Earthquake Engineering*, Lisbon, Portugal.

- Jiang, H., and Kurama, Y. C. (2010). "Analytical modeling of medium-rise reinforced concrete shear walls." *ACI Struct. J.*, 107(4), 400–410.
- Kolozvari, K. (2013). "Analytical modeling of cyclic shear-flexure interaction in reinforced concrete structural walls." Ph.D. dissertation, Univ. of California, Los Angeles.
- Kolozvari, K., Orakcal, K., and Wallace, J. W. (2014). "Modeling of cyclic shear-flexure interaction in reinforced concrete structural walls. Part I: Theory." *J. Struct. Eng.*, 10.1061/(ASCE)ST.1943-541X.0001059, 04014135.
- Mander, J. B., Priestley, M. J. N., and Park, R. (1988). "Theoretical stress-strain model for confined concrete." *J. Struct. Eng.*, 10.1061/(ASCE)0733-9445(1988)114:8(1804), 1804–1826.
- Mansour, M. Y., Hsu, T. C., and Lee, J. Y. (2002). "Pinching effect in hysteretic loops of R/C shear elements." *ACI Spec. Publ.*, 205, 293–322.
- Massone, L. M., Orakcal, K., and Wallace, J. W. (2006). "Shear-flexure interaction for structural walls." *ACI Special Publication, Deformation capacity and shear strength of reinforced concrete members under cyclic loading*, SP-236, American Concrete Institute (ACI), Farmington Hill, MI, 127–150.
- Massone, L. M., Orakcal, K., and Wallace, J. W. (2009). "Modeling of squat structural walls controlled by shear." *ACI Struct. J.*, 106(5), 646–655.
- Massone, L. M., and Wallace, J. W. (2004). "Load-deformation responses of slender reinforced concrete walls." *ACI Struct. J.*, 101(1), 103–113.
- Matlab* [Computer software]. MathWorks, Natick, MA.
- McKenna, F., Fenves, G. L., Scott, M. H., and Jeremic, B. (2000). "Open system for earthquake engineering simulation (OpenSees)." Pacific Earthquake Engineering Research Center, Univ. of California, Berkeley, CA.
- Menegotto, M., and Pinto, E. (1973). "Method of analysis for cyclically loaded reinforced concrete plane frames including changes in geometry and non-elastic behavior of elements under combined normal force and bending." *Proc., IABSE Symp. on Resistance and Ultimate Deformability of Structures Acted on by Well-Defined Repeated Loads*, IABSE, ETH Zurich, Zurich, Switzerland, 15–22.
- Oosterle, R. G., Aristizabal-Ochoa, J. D., Fiorato, A. E., Russell, H. G., and Corley, W. G. (1979). "Earthquake resistant structural walls: Tests of isolated walls, phase II." *Rep. to National Science Foundation*, PCA Construction Technology Laboratories, Skokie, IL, 332.
- Oosterle, R. G., Fiorato, A. E., Johal, L. S., Carpenter, J. E., Russell, H. G., and Corley, W. G. (1976). "Earthquake resistant structural walls: Tests of isolated walls." *Rep. to National Science Foundation*, PCA Construction Technology Laboratories, Skokie, IL, 317.
- Orakcal, K., Ulugtekin, D., and Massone, L. M. (2012). "Constitutive modeling of reinforced concrete panel behavior under cyclic loading." *Proc., 15th World Conf. on Earthquake Engineering*, Lisbon, Portugal.
- Orakcal, K., and Wallace, J. W. (2006). "Flexural modeling of reinforced concrete walls: Experimental verification." *ACI Struct. J.*, 103(2), 196–206.
- Orakcal, K., Wallace, J. W., and Conte, J. P. (2004). "Flexural modeling of reinforced concrete walls: Model attributes." *ACI Struct. J.*, 101(5), 688–698.
- Panagiotou, M., Restrepo, J., Schoettler, M., and Kim, G. (2011). "Non-linear cyclic truss model for reinforced concrete walls." *ACI Struct. J.*, 109(2), 205–214.
- Petrangeli, M., Pinto, P. E., and Ciampi, V. (1999). "Fiber element for cyclic bending and shear of RC structures. I: Theory." *J. Eng. Mech.*, 10.1061/(ASCE)0733-9399(1999)125:9(994), 994–1001.
- Saatcioglu, M., and Razvi, S. R. (1992). "Strength and ductility of confined concrete." *J. Struct. Eng.*, 10.1061/(ASCE)0733-9445(1992)118:6(1590), 1590–1607.
- Tran, T. A. (2012). "Experimental and analytical studies of moderate aspect ratio reinforced concrete structural walls." Ph.D. dissertation, Univ. of California, Los Angeles.
- Tran, T. A., and Wallace, J. W. (2012). "Experimental study of nonlinear flexural and shear deformations of reinforced concrete structural walls." *Proc., 15th World Conf. on Earthquake Engineering*, Lisbon, Portugal.
- Ulugtekin, D. (2010). "Analytical modeling of reinforced concrete panel elements under reversed cyclic loadings." M.S. thesis, Bogazici Univ., Istanbul, Turkey.
- Valluvan, R., Kreger, M. E., and Jirsa, J. O. (1999). "Evaluation of ACI 318-95 shear friction provisions." *ACI Struct. J.*, 96(4), 473–481.
- Vecchio, F. J., and Collins, M. P. (1993). "Compression response of cracked reinforced concrete." *J. Struct. Eng.*, 10.1061/(ASCE)0733-9445(1993)119:12(3590), 219–231.
- Vulcano, A., and Bertero, V. V. (1987). "Analytical models for predicting the lateral response of RC shear walls: Evaluation of their reliability." *EERC Rep. No. UCB/EERC-87/19*, Earthquake Engineering Research Center, Univ. of California, Berkeley, CA, 99.
- Vulcano, A., Bertero, V. V., and Colotti, V. (1988). "Analytical modeling of RC structural walls." *Proc., 9th World Conf. on Earthquake Engineering*, Vol. 6, Tokyo, Japan, 41–46.
- Wood, L. S. (1990). "Shear strength of low-rise reinforced concrete walls." *ACI Struct. J.*, 87(1), 99–107.